

# Frequency Response Analysis of Load Effect on Dynamics of Grid-Forming Inverter

Matias Berg\*, Tuomas Messo, Teuvo Suntio

Laboratory of Electrical Energy Engineering, Tampere University of Technology, Tampere, Finland

\*E-mail: matias.berg@tut.fi

**Abstract**—The grid-forming mode of the voltage source inverters (VSI) is applied in uninterruptible power supplies and micro-grids to improve the reliability of electricity distribution. During the intentional islanding of an inverter-based micro-grid, the grid-forming inverters (GFI) are responsible for voltage control, similarly as in the case of uninterruptible power supplies (UPS). The unterminated model of GFI can be developed by considering the load as an ideal current sink. Thus, the load impedance always affects the dynamic behavior of the GFI. This paper proposes a method, to analyze how the dynamics of GFI and the controller design are affected by the load. Particularly, how the frequency response of the voltage loop gain changes according to the load and, how it can be used to predict time-domain step response. The frequency responses that are measured from a hardware-in-the-loop simulator are used to verify and illustrate explicitly the load effect.

**Keywords**—grid-forming inverter, dynamics, dq-domain, load effect

## I. INTRODUCTION

The recent years have witnessed a huge growth in the number of installed distributed photovoltaic generation systems. Distributed generation with an energy storage system in a micro-grid enables the intentional islanding of the micro-grid during a failure in the utility network [1], [2]. If there are no rotating generators in the micro-grid, the inverters that normally operate in the grid-feeding mode, have to form the grid during the intentional islanding [3]. The dynamics of the grid-forming inverter (GFI) differ from the dynamics of the grid-feeding inverter. The grid-forming inverter is a voltage-output converter and the grid-feeding inverter is a current-output converter [4]. An ideal current sink as the load of GFI is the basis for the dynamic analysis, but the load effect has to be taken into account.

The importance of modeling the output impedance of power-electronics-based systems has been widely addressed [5]–[7]. In order to derive the output impedance, the output current has to be considered an input variable. The output impedance has been derived this way in [5]. The output impedance modeled in [5] is verified by frequency response measurements, but the other transfer functions are not measured. Dynamics of an LC-filter has been included to the input admittance of an active rectifier for the purposes of impedance-based analysis in [8]. Passive loads have been modeled as a part of a system consisting of grid-connected solar inverter and an active rectifier in [9]. However, the analysis is focused on the frequency responses of impedances and the effect of

the filter on control-to-output transfer functions was not analyzed in [8], [9].

The control-related transfer functions change if the load is changed from a current sink to a passive or active load. The output impedance of the grid-forming inverter has been derived also in [10] and the output current is considered as an input variable. The unterminated dynamics are analyzed when the controllers are tuned. However, the simulation and practical tests are done with passive and non-linear loads without analyzing the load effect to the control loops. In [11] the output current of a single-phase system is considered as an input variable and the unterminated model is used to derive the transfer functions. The time-domain behavior is tested under a resistive load and a non-linear load. However, the load effect on the loop gains is not shown.

A load-affected transfer function is directly derived in phase domain in [1]. However, no frequency-response verification is presented. A dynamic model of a passive load is derived in [12], but it is not used for frequency response analysis of the system. In [2] the load is analyzed in the dq-domain and included in the system model, but frequency response analysis is missing. A passive load has been addressed also in [13] and [14], but no frequency responses are analyzed.

This paper proposes a method, that can be used to analyze the load effect on the unterminated dynamics of GFI in the frequency domain. The rest of the paper is organized as follows: Section II introduces the modeling of the unterminated dynamics of the three-phase grid-forming inverter in dq-domain. Section III examines the load effect on the dynamics of GFI. Frequency response analysis of the load effect is used to tune the controllers and to predict the time-domain response in Section IV. The conclusions are finally presented in Section V.

## II. UNTERMINATED SMALL-SIGNAL MODEL

The used averaging and linearizing method originates from the work of Middlebrook [15]. Figure 1 shows the circuit diagram of a three-phase grid-forming inverter. The load is assumed to be an ideal three phase current sink in the dynamic analysis. Thus, the grid inductance or load side inductors of the LCL-filter cannot be included in the unterminated models due to violation of Kirchoff's law. Output impedance of the grid-forming inverter and the other input-to-output transfer function can be derived by analyzing the power stage in Fig. 1. The input variables are input voltage, duty-ratios and output currents. The

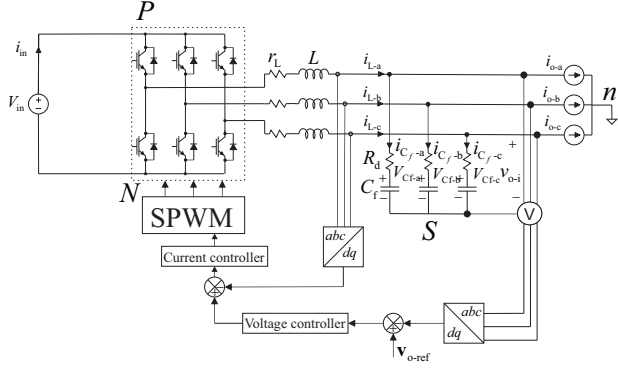


Figure 1. Circuit diagram of the grid-forming inverter including a simplified control system.

output variables are input current, inductor currents and output voltages. The inductor currents are chosen as output variables, because they are commonly needed in the cascaded control of the output voltage.

A state-space model of the grid-forming inverter is derived. The capacitor voltages and inductor currents are chosen as the state variables. Modeling in the synchronous reference frame is applied. For brevity, the equations are shown directly in the synchronous reference frame (DQ-frame). In the following equations, subscripts d and q denote whether the corresponding variable is either the direct or quadrature component.  $i_L$  is the inductor current,  $i_o$  the output current,  $d$  the duty ratio,  $v_{in}$  the input voltage,  $v_{Cf}$  the filter capacitor voltage,  $i_{in}$  the input current. Angle brackets around the variables in (1)–(7) denote that equations are averaged over one switching period. Thus, on and off-time equations are not shown separately.

$$\langle i_{in} \rangle = \frac{3}{2} (d_d \langle i_{Ld} \rangle + d_q \langle i_{Lq} \rangle) \quad (1)$$

$$\frac{d \langle i_{Ld} \rangle}{dt} = \frac{1}{L} [d_d \langle v_{in} \rangle - (r_L + r_{sw} + R_d) \langle i_{Ld} \rangle + \omega_s i_{Lq} + R_d \langle i_{od} \rangle - \langle v_{Cfd} \rangle] \quad (2)$$

$$\frac{d \langle i_{Lq} \rangle}{dt} = \frac{1}{L} [d_q \langle v_{in} \rangle - (r_L + r_{sw} + R_d) \langle i_{Lq} \rangle - \omega_s i_{Ld} + R_d \langle i_{oq} \rangle - \langle v_{Cfq} \rangle] \quad (3)$$

$$\frac{d \langle v_{Cfd} \rangle}{dt} = \frac{1}{C_f} [\langle i_{Ld} \rangle + \omega_s v_{Cfq} - \langle i_{od} \rangle] \quad (4)$$

$$\frac{d \langle v_{Cfq} \rangle}{dt} = \frac{1}{C_f} [\langle i_{Lq} \rangle - \omega_s v_{Cfd} - \langle i_{oq} \rangle] \quad (5)$$

$$\langle v_{od} \rangle = \langle v_{Cfd} \rangle + R_d \langle i_{Ld} \rangle - R_d \langle i_{od} \rangle \quad (6)$$

$$\langle v_{oq} \rangle = \langle v_{Cfq} \rangle + R_d \langle i_{Lq} \rangle - R_d \langle i_{oq} \rangle, \quad (7)$$

where  $C_f$ ,  $L$ ,  $d$ ,  $r_{sw}$  and  $\omega_s$  denote filter capacitor, filter inductor, duty ratio, parasitic resistance of a switch, grid angular frequency, respectively.  $r_L$  is the equivalent series resistance of the filter inductor. The damping resistance that includes the filter capacitor equivalent series resistance is denoted by  $R_D$ . Capital letters denote steady-state values at the operating point.

Equations (1)–(7) are linearized at the steady-state operation point and transformed into the frequency domain. The linearized equations are expressed by coefficient matrices **A**, **B**, **C** and **D**, input variable vector **U**, output variable vector **Y** and state variable vector **X**. Equation (8) shows the state space after transformation to frequency domain using the Laplace variable 's' and the output and input variable vectors are shown in (9) and (10), respectively.

$$\begin{aligned} s\mathbf{X}(s) &= \mathbf{A}\mathbf{X}(s) + \mathbf{B}\mathbf{U}(s) \\ \mathbf{Y}(s) &= \mathbf{C}\mathbf{X}(s) + \mathbf{D}\mathbf{U}(s) \end{aligned} \quad (8)$$

The coefficient matrices are shown in (11)–(14).

$$\mathbf{Y} = [\hat{i}_{in} \quad \hat{i}_{Ld} \quad \hat{i}_{Lq} \quad \hat{v}_{od} \quad \hat{v}_{oq}]^T \quad (9)$$

$$\mathbf{U} = [\hat{v}_{in} \quad \hat{i}_{od} \quad \hat{i}_{oq} \quad \hat{d}_d \quad \hat{d}_q]^T \quad (10)$$

$$\mathbf{A} = \begin{bmatrix} -\frac{r_{eq}}{L} & \omega_s & -\frac{1}{L} & 0 \\ -\omega_s & -\frac{r_{eq}}{L} & 0 & -\frac{1}{L} \\ \frac{1}{C_f} & 0 & 0 & \omega_s \\ 0 & \frac{1}{C_f} & -\omega_s & 0 \end{bmatrix} \quad (11)$$

$$\mathbf{B} = \begin{bmatrix} \frac{D_d}{L} & \frac{R_d}{L} & 0 & \frac{V_{in}}{L} & 0 \\ \frac{D_q}{L} & 0 & \frac{R_d}{L} & 0 & \frac{V_{in}}{L} \\ 0 & -\frac{1}{C_f} & 0 & 0 & 0 \\ 0 & 0 & -\frac{1}{C_f} & 0 & 0 \end{bmatrix} \quad (12)$$

$$\mathbf{C} = \begin{bmatrix} \frac{3D_d}{2} & \frac{3D_q}{2} & 0 & 0 \\ 1 & 0 & 0 & 0 \\ 0 & 1 & 0 & 0 \\ R_d & 0 & 1 & 0 \\ 0 & R_d & 0 & 1 \end{bmatrix} \quad (13)$$

$$\mathbf{D} = \begin{bmatrix} 0 & 0 & 0 & \frac{3I_{Ld}}{2} & \frac{3I_{Lq}}{2} \\ 0 & 0 & 0 & 0 & 0 \\ 0 & 0 & 0 & 0 & 0 \\ 0 & -R_d & 0 & 0 & 0 \\ 0 & 0 & -R_d & 0 & 0 \end{bmatrix}, \quad (14)$$

where  $r_{eq}$  denotes  $r_L + r_{sw} + R_d$ . The transfer functions from the inputs to the outputs can be solved as shown in (15).

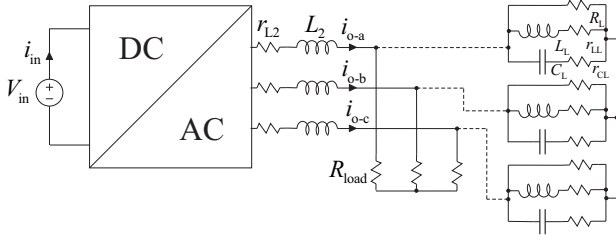


Figure 2. Circuit diagram of the grid-forming inverter including the load-side inductor and a resistive load or alternatively a RLC-load.

$$\mathbf{Y}(s) = \overbrace{(\mathbf{C}(s\mathbf{I} - \mathbf{A})^{-1}\mathbf{B} + \mathbf{D})}^{\mathbf{G}} \mathbf{U}(s), \quad (15)$$

where matrix  $\mathbf{G}$  contains the transfer functions. Different transfer functions can be collected from the matrix as shown in (16).

$$\begin{bmatrix} Y_{in} & T_{oid} & T_{oiq} & G_{cid} & G_{ciq} \\ G_{ioLd} & G_{oLd} & G_{oLqd} & G_{cLd} & G_{cLqd} \\ G_{ioLq} & G_{oLdq} & G_{oLq} & G_{cLdq} & G_{cLq} \\ G_{iod} & -Z_{od} & -Z_{oqd} & G_{cod} & G_{coqd} \\ G_{ioq} & -Z_{oqd} & -Z_{oq} & G_{codq} & G_{coq} \end{bmatrix} \quad (16)$$

In this paper the transfer functions are merged into transfer matrices [5], [16]. Equation (17) shows the transfer matrices that were solved in (15) and the corresponding input and output variables. Hats over the input and output variables denote small-signal variables. Input voltage and input current are scalar variables and their small signal dependency is denoted by  $Y_{in}$ . The input and output variables that are collected into 2-by-1 vectors are shown in (18).

$$\begin{bmatrix} \hat{v}_{in} \\ \hat{\mathbf{i}}_L \\ \hat{\mathbf{v}}_o \end{bmatrix} = \begin{bmatrix} Y_{in} & \mathbf{T}_{oi} & \mathbf{G}_{ci} \\ \mathbf{G}_{iL} & \mathbf{G}_{oL} & \mathbf{G}_{cL} \\ \mathbf{G}_{io} & -\mathbf{Z}_o & \mathbf{G}_{co} \end{bmatrix} \begin{bmatrix} \hat{v}_{in} \\ \hat{\mathbf{i}}_o \\ \hat{\mathbf{d}} \end{bmatrix} \quad (17)$$

$$\begin{aligned} \hat{\mathbf{i}}_L &= [\hat{v}_{Ld} \quad \hat{v}_{Lq}]^T \hat{\mathbf{v}}_o = [\hat{v}_{od} \quad \hat{v}_{oq}]^T \\ \hat{\mathbf{i}}_o &= [\hat{v}_{od} \quad \hat{v}_{oq}]^T \hat{\mathbf{d}} = [\hat{d}_d \quad \hat{d}_q]^T \end{aligned} \quad (18)$$

### III. LOAD EFFECT

Grid-feeding inverters are commonly equipped with an LCL-filter. It is assumed that an inverter that is used in the grid-feeding mode will be used also in the grid-forming mode. In the case of grid-feeding inverters, load impedances have been included in the model in [17] and analytical equations for generalized source and load interactions are shown in [4]. The effect of load dynamics on the unterminated dynamics has been analyzed in the case of DC-DC converters in [18]. Fig. 2 shows a circuit diagram of the grid-forming inverter, where the load is a resistor or alternatively a parallel RLC-load (as depicted

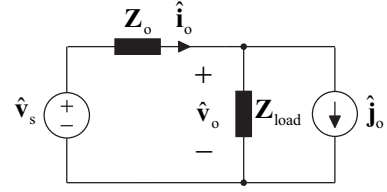


Figure 3. An equivalent small-signal circuit that has been widely used to analyze to impedance based stability.

using dashed lines). The load-side inductor is taken into account in the model. In the unterminated model in Fig. 1 the load-side inductor is not included, because the series connection of an inductor and current sink is inconsistent according to circuit theory.

Fig. 3 shows an equivalent small-signal circuit of two interconnected systems. Very similar circuits have been widely used in the literature for impedance-based stability analysis [7], [9], [19], [20]. Variables  $\hat{v}_s$  and  $\hat{\mathbf{j}}_o$  denote small-signal source voltage and load current, respectively. However, they do not indicate, how the voltage and current are dependent on the inverter input parameters. In following, the general voltage source is replaced by the control-to-output transfer function matrices so that the load-affected transfer functions can be solved.

The output dynamics of the grid-forming inverter are shown as an equivalent linear circuit in Fig. 4(a) which corresponds to the equation of  $\hat{v}_o$  in (17) that is developed from the case the load is an ideal current sink in Fig. 1. However, the load effect of the load-side inductor, its ESR and the load resistor in Fig. 2 must be taken into account. Figure 4(b) shows the output dynamics model, where the load impedance  $\mathbf{Z}_{load}$  and the impedance of the load-side inductor  $\mathbf{Z}_{L2}$  are included. The transfer functions for the load and the inductor impedance are derived similarly as the unterminated model. Appendix A shows the state-space coefficient matrices that are used to solve as the admittance matrix of the grid-side inductor. The inverse of the admittance matrix is  $\mathbf{Z}_{L2}$ . Appendix B shows the coefficient matrices for the RLC-load. Equations for the small-signal output voltage  $\hat{v}_o$  are written for the both circuits in Figs. 4(a) and 4(b). The equations are shown in (19) and (20), respectively.

$$\hat{\mathbf{v}}_o = \mathbf{G}_{io}\hat{v}_{in} - \mathbf{Z}_o\hat{\mathbf{i}}_o + \mathbf{G}_{co}\hat{\mathbf{d}} \quad (19)$$

$$\hat{\mathbf{v}}_o = \mathbf{Z}_{L2}\hat{\mathbf{i}}_o + \mathbf{Z}_{load}\hat{\mathbf{i}}_o - \mathbf{Z}_{load}\hat{\mathbf{j}}_o \quad (20)$$

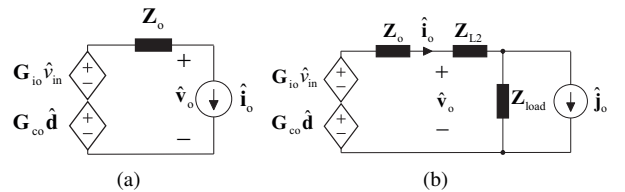


Figure 4. a) Output dynamics and b) load-affected output dynamics.

Small-signal output current vector  $\hat{\mathbf{i}}_o$  is solved from (20). The solution is shown in (21).

$$\hat{\mathbf{i}}_o = (\mathbf{Z}_{L2} + \mathbf{Z}_{load})^{-1} \hat{\mathbf{v}}_o + (\mathbf{Z}_{L2} + \mathbf{Z}_{load})^{-1} \mathbf{Z}_{load} \hat{\mathbf{j}}_o \quad (21)$$

Eq. (22) shows the result when  $\hat{\mathbf{i}}_o$  in (21) is substituted to (19). The  $(\mathbf{I} + \mathbf{Z}_o(\mathbf{Z}_{L2} + \mathbf{Z}_{load})^{-1})^{-1}$  is the common factor in all of the equations. The load-affected control-to-output transfer functions are collected from the bottom row of the matrix in (27). The transfer functions from  $\hat{\mathbf{j}}_o$  to  $\hat{\mathbf{v}}_o$  could be also manipulated to (23). This format shows that the small-signal current  $\hat{\mathbf{i}}_o$  is solved analogously to circuit theory by dividing  $\hat{\mathbf{j}}_o$  according to the impedances and the multiplying by  $-\mathbf{Z}_o$  to solve the output voltage  $\hat{\mathbf{v}}_o$ .

$$\hat{\mathbf{v}}_o = (\mathbf{I} + \mathbf{Z}_o(\mathbf{Z}_{L2} + \mathbf{Z}_{load})^{-1})^{-1} (\mathbf{G}_{io} \hat{\mathbf{v}}_{in} - \mathbf{Z}_o(\mathbf{Z}_{L2} + \mathbf{Z}_{load})^{-1} \mathbf{Z}_{load} \hat{\mathbf{j}}_o + \mathbf{G}_{co} \hat{\mathbf{d}}) \quad (22)$$

$$\hat{\mathbf{v}}_o = -(\mathbf{Z}_o + \mathbf{Z}_{L2} + \mathbf{Z}_{load})^{-1} \mathbf{Z}_{load} \mathbf{Z}_{co} \hat{\mathbf{j}}_o \quad (23)$$

The control-to-output voltage transfer function  $\mathbf{G}_{co}^L$  can be solved also directly from the load affected output dynamics diagram in Fig. 4(b). The load affected circuit can be understood as a voltage divider, which divides the small-signal voltage caused by  $\mathbf{G}_{co}$  or  $\mathbf{G}_{io}$  over the impedances  $\mathbf{Z}_o$ ,  $\mathbf{Z}_{L2}$  and  $\mathbf{Z}_{load}$ . A very similar equations has been analyzed in [19], [20]. However, in [19], [20] the equations are derived in the case of an arbitrary voltage source as in Fig. 3 – not in the case of input-output dynamics of the converter.

The remaining load-affected transfer functions in (27) are solved by substituting  $\hat{\mathbf{i}}_o$  in (17) by (21) as shown in (24) and then substituting  $\hat{\mathbf{v}}_o$  by (22). Solving for  $\hat{i}_{in}$  and  $\hat{\mathbf{i}}_L$  as a function of  $\hat{v}_{in}$ ,  $\hat{\mathbf{j}}_o$  and  $\hat{\mathbf{d}}$  gives the load affected transfer functions. Equation (25) shows the result in the case of inductor current. Load-affected output transfer functions  $\mathbf{G}_{io}^L$ ,  $\mathbf{G}_o^L$  and  $\mathbf{G}_{co}^L$  are used for brevity in (25) instead of using the expression in (22). The load affected input current dynamics (26) can be solved similarly as the load affected inductor current dynamics.

$$\hat{\mathbf{i}}_L = \mathbf{G}_{iL} \hat{v}_{in} + \mathbf{G}_{oL} ((\mathbf{Z}_{L2} + \mathbf{Z}_{load})^{-1} \hat{\mathbf{v}}_o + (\mathbf{Z}_{L2} + \mathbf{Z}_{load})^{-1} \mathbf{Z}_{load} \hat{\mathbf{j}}_o) + \mathbf{G}_{cL} \hat{\mathbf{d}} \quad (24)$$

$$\hat{\mathbf{i}}_L = (\mathbf{G}_{iL} + \mathbf{G}_{oL}(\mathbf{Z}_{L2} + \mathbf{Z}_{load})^{-1} \mathbf{G}_{io}^L) \hat{v}_{in} + (\mathbf{G}_{cL} + \mathbf{G}_{oL}(\mathbf{Z}_{L2} + \mathbf{Z}_{load})^{-1} \mathbf{G}_{co}^L) \hat{\mathbf{d}} + \mathbf{G}_{oL}((\mathbf{Z}_{L2} + \mathbf{Z}_{load})^{-1} \mathbf{Z}_{load} - ((\mathbf{Z}_{L2} + \mathbf{Z}_{load})^{-1} (-\mathbf{G}_o^L))) \hat{\mathbf{j}}_o \quad (25)$$

$$\hat{i}_{in} = (Y_{in} + \mathbf{T}_{oi}(\mathbf{Z}_{L2} + \mathbf{Z}_{load})^{-1} \mathbf{G}_{io}^L) \hat{v}_{in} + (\mathbf{G}_{ci} + \mathbf{T}_{oi}(\mathbf{Z}_{L2} + \mathbf{Z}_{load})^{-1} \mathbf{G}_{co}^L) \hat{\mathbf{d}} + \mathbf{T}_{oi}((\mathbf{Z}_{L2} + \mathbf{Z}_{load})^{-1} \mathbf{Z}_{load} - ((\mathbf{Z}_{L2} + \mathbf{Z}_{load})^{-1} (-\mathbf{G}_o^L))) \hat{\mathbf{j}}_o \quad (26)$$

$$\begin{bmatrix} \hat{i}_{in} \\ \hat{\mathbf{i}}_L \\ \hat{\mathbf{v}}_o \end{bmatrix} = \begin{bmatrix} Y_{in}^L & \mathbf{T}_{oi}^L & \mathbf{G}_{ci}^L \\ \mathbf{G}_{iL}^L & \mathbf{G}_{oL}^L & \mathbf{G}_{cL}^L \\ \mathbf{G}_{io}^L & -\mathbf{G}_o^L & \mathbf{G}_{co}^L \end{bmatrix} \begin{bmatrix} \hat{v}_{in} \\ \hat{\mathbf{j}}_o \\ \hat{\mathbf{d}} \end{bmatrix} \quad (27)$$

The resulting load-affected dynamics can be expressed as shown in (27), where superscript L denotes that the transfer functions are affected by the load impedance. It should be noted that  $\hat{\mathbf{j}}_o$  replaces  $\hat{\mathbf{i}}_o$  as an input variable as it can be seen from Fig. 4(b). Since  $\hat{\mathbf{j}}_o$  and  $\hat{\mathbf{v}}_o$  are not defined at an interface according to the definition of an impedance, a transfer function matrix  $\mathbf{G}_o^L$  is used instead of an impedance matrix.

References [21] and [22] have pointed out that the impedances of interconnected three-phase systems should be shifted to a global reference frame to enable impedance-based stability analysis. However, the load impedance matrix of the pure resistive load and the RLC-load analyzed in this paper are symmetric, which means that no impedance shifting is required.

#### IV. FREQUENCY RESPONSE ANALYSIS

The parameters and the operating point values of the grid-forming inverter are shown in Tables I and II. The resistive load in Fig. 2 is considered first. Fig. 6 shows both the frequency response given by analytical model  $G_{cod}^L$  and the frequency response measured from a hardware-in-the-loop simulator.  $G_{cod}^L$  is the transfer function from the duty ratio d-component to the output voltage d-component, which has major importance for control design. The resistive load  $R_{load}$  is chosen according to (28) so that nominal operation point is maintained. Eq. (29) shows, how the load impedance matrix is defined in the case of the resistive load.

$$R_{load} = \frac{V_{od}}{I_{od}} - r_{L2} \quad (28)$$

$$\mathbf{Z}_{load} = \begin{bmatrix} R_{load} & 0 \\ 0 & R_{load} \end{bmatrix} \quad (29)$$

Table I. INVERTER PARAMETER VALUES

Parameter	Value	Parameter	Value
$L$	1.4 mH	$r_L$	25 mΩ
$L_2$	0.47 mH	$r_{L2}$	22 mΩ
$C_f$	10 μF	$R_d$	1.96 Ω
$f_s$	10 kHz	$r_{sw}$	10 mΩ
$\omega_s$	2π60 Hz		

Table II. OPERATING POINT VALUES

Parameter	Value	Parameter	Value
$V_{od}$	169.7 V	$V_{oq}$	0.0000 V
$I_{od}$	19.64 A	$I_{oq}$	0.0000 A
$I_{Ld}$	19.65 A	$I_{Lq}$	0.6397 A
$V_{Cfd}$	169.7 V	$V_{Cfq}$	-1.254 V
$V_{in}$	416.0 V	$I_{in}$	16.93 A
$D_d$	0.4088	$D_q$	0.0250

The correlation between the measured and predicted based frequency responses in Fig. 6 confirms that the proposed model is correct. The mainly resistive load damps the resonance caused by the LC-filter. The instruments utilized in the measurements were Typhoon HIL -real time simulator, Boombox control platform from Imperix and Venable frequency response analyzer. A photograph of the HIL simulation setup is shown in Fig. 5. An oscilloscope was used additionally.

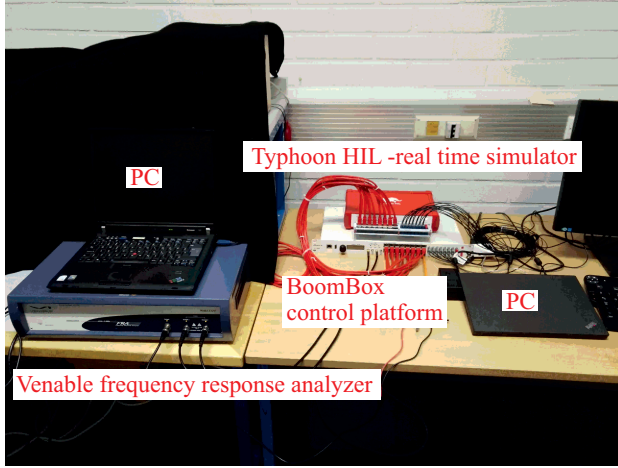


Figure 5. Real-time simulation setup: PC, Venable frequency response analyzer, Boombox control platform, and Typhoon HIL -real time simulator.

Taking advantage of the steps to derive the load-affected transfer function, the load effect can be also removed from the frequency response. Eq. (30) shows, how  $G_{co}$  can be calculated if the load-affected transfer function matrix,  $G_{co}^L$  is known from measurements, i.e., the unterminated dynamic model can be solved even if the load is not an ideal current sink.

$$G_{co} = (I + Z_o(Z_{L2} + Z_{load})^{-1})G_{co}^L \quad (30)$$

Fig. 6 shows also a comparison between the derived  $G_{cod}$  in (17) and the transfer function calculated according to (30).  $G_{cod}$  corresponds to the situation of Fig. 1, where the load is an ideal current sink. Thus, the ideal transfer functions can be illustrated even though, the converter is affected by the load impedance. Assuming that the impedance matrices  $Z_o$ ,  $Z_{L2}$  and  $Z_{Load}$  are known.

A cascaded controller is commonly used to control the output voltage of the grid-forming inverter [5], [23], [24]. The controller consists of the inner inductor current loop

and outer output voltage loop. The controller is tuned according to the control-to-inductor-current and control-to-output voltage transfer functions affected by the R-load. Fig. 7 shows the measured and model-based frequency response of the  $G_{cLd}^L$ . The unterminated control-to-current d-component  $G_{cLd}$  is also shown in Fig. 7. The resistive load clearly damps the resonance and increases the low-frequency gain, which greatly simplifies the tuning of the current controller. The current controller  $G_{cc}$  is a PI-controller. Consisting of an integrator, a zero at 1 kHz and a gain of 36.8 dB.

Fig. 8 shows the frequency response of the full-order current loop gain  $L_{outCd}^{FO}$ . The phase margin is 65.4° at 551 Hz. The gain margin is 8.51 dB. The full-order current loop gain includes the cross-coupling between d and q-components. The loop gain is given in (31) and it has been derived in [4]. The delay caused by sampling and PWM is  $1.5/f_s$  and it is modeled by a third order Padé approximation [16]. The delay transfer function is omitted for brevity from (31), but it is shown in (32) and in completed block diagram of the system in Fig. 11.

$$L_{outCd}^{FO} = G_{cLd}^L G_{cc} - \frac{G_{cLqd}^L G_{cLqd}^L}{1 + G_{cLq}^L G_{cc}} G_{cc} G_{cc} \quad (31)$$

The matrix current loop gain is shown in (32).

$$L_{outC} = G_{cL} G_{del} G_{cc} G_{seC} \quad (32)$$

The current loop is closed in (33) and (34) shows, how the inductor current reference-to-output voltage transfer function  $G_{co}^{sec}$  is calculated. Superscript 'sec' denotes secondary and means that the secondary control loop (i.e. current loop) is closed.  $G_{cod}^{sec}$  is used to tune the voltage controller. Fig. 11 shows the control block diagram of the complete system. The block diagram can be used to calculate also other closed-loop transfer functions and loop gains.

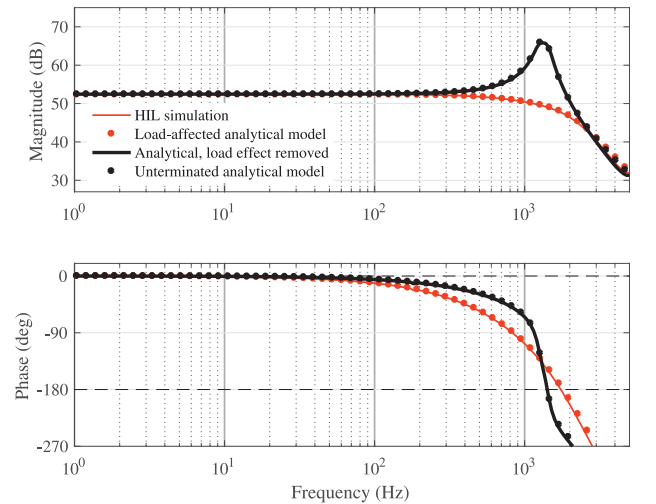


Figure 6. Measured and model-based frequency responses of  $G_{cod}^L$  (resistive load).

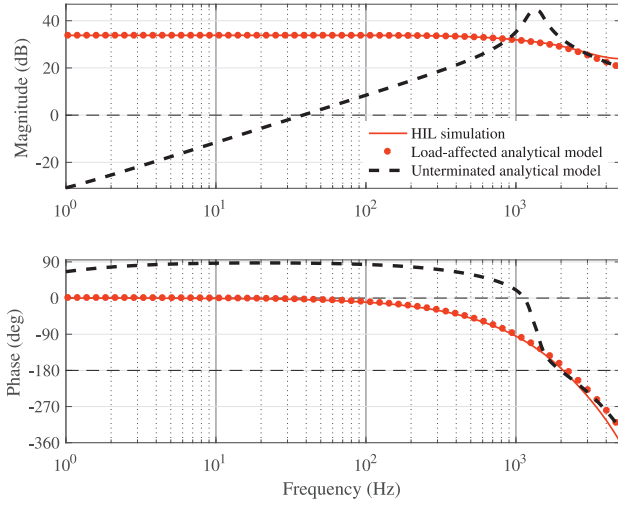


Figure 7. Bode plot of HIL-simulated and derived  $G_{cLd}^L$  for the R-load and the unterminated  $G_{cLd}$ .

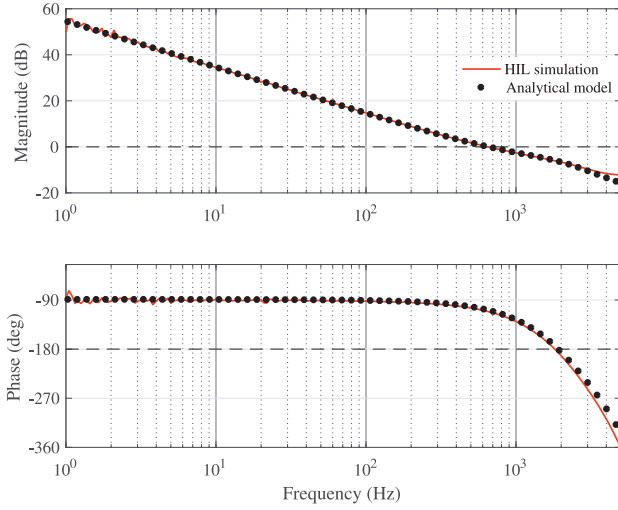


Figure 8. Bode plot of measured and derived current loop gain  $L_{outCd}^{FO}$  for the R-load.

$$\mathbf{G}_{cL}^{sec} = (\mathbf{I} + \mathbf{L}_{outC})^{-1} \mathbf{G}_{cL}^L \mathbf{G}_{del} \mathbf{G}_{cc} \quad (33)$$

$$\mathbf{G}_{co}^{sec} = \mathbf{G}_{co}^L \mathbf{G}_{del} \mathbf{G}_{cc} - \mathbf{G}_{co}^L \mathbf{G}_{cL}^{-1} \mathbf{L}_{outC} \mathbf{G}_{cL}^{sec} \quad (34)$$

$$L_{outV-d}^{FO} = G_{cod}^L G_{vc} - \frac{G_{coqd}^L G_{coqd}^L}{1 + G_{coq}^L G_{vc}} G_{vc} G_{vc} \quad (35)$$

Fig. 9 shows the simulated and the frequency response of the analytic voltage loop gain  $L_{outVd}^{FO}$  (35) and the model of  $G_{cod}^{sec}$ . The crossover frequency the voltage loop is 53.9 Hz and the phase margin is 93.5 ° when the load is pure resistance. The voltage controller  $G_{vc}$  consists of an integrator, a zero at 200 Hz, a pole at 600 Hz and a gain of 31.6 dB.

The cascaded controller is kept unchanged, but the

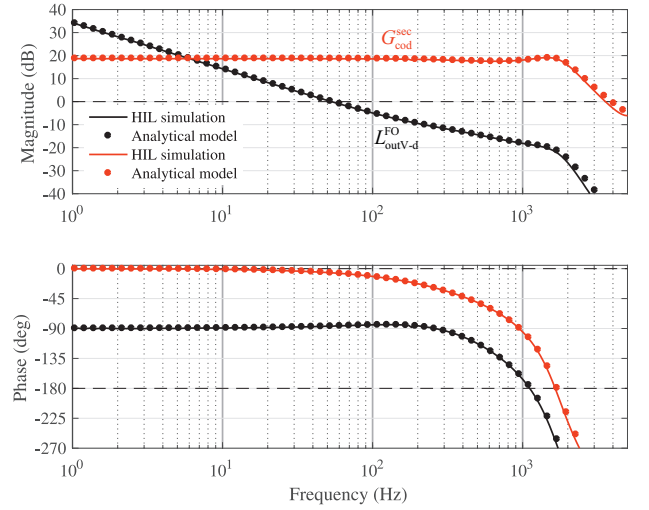


Figure 9. Bode plot of simulated and derived voltage controller loop gain  $L_{outVd}^{FO}$  and the current loop affected control-to-output dynamics  $G_{cod}^{Lsec}$ .

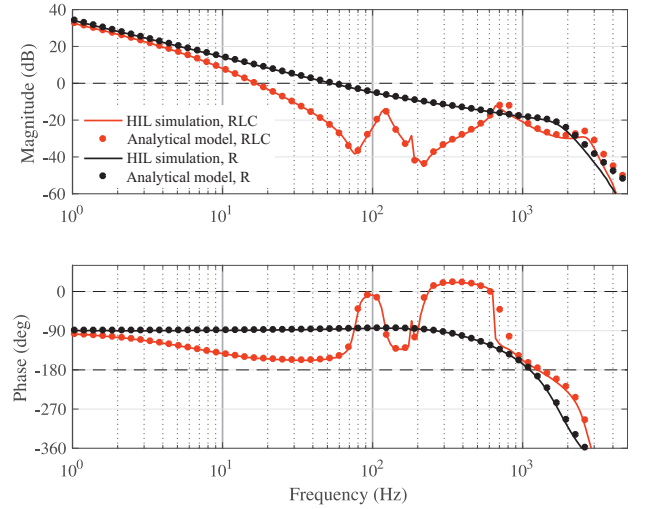


Figure 10. Bode plot of measured and derived voltage controller loop gain  $L_{outVd}^{FO}$  for the R-load and for the RLC-load.

load is changed to the RLC-load that is similar to the RLC-load used in [13].  $L_L$  and  $C_L$  are 4.584 mH and 1.535 mF, respectively. The resonance frequency is at around 60 Hz as in [13]. 30 mΩ resistances  $r_{LL}$  and  $r_{CL}$  are connected in series with the parallel capacitance and inductance, respectively.  $R_L$  of the parallel load equals  $R_{load}$ , the load of the first case. Figure 10 shows also the frequency response of the voltage loop in this case. It can be seen that the crossover frequency is 16.5 Hz and the phase margin is reduced to 26.7 °. The low phase margin indicates that there will be oscillation in the step response of the system.

A step response comparison by using the R and RLC-loads is done. The system is simulated in Typhoon HIL as in the case of frequency-domain measurement. An oscilloscope is connected to the analog outputs of Imperix Boombox to analyze the response in detail in dq-domain. Fig. 12 shows the output voltage response to a step

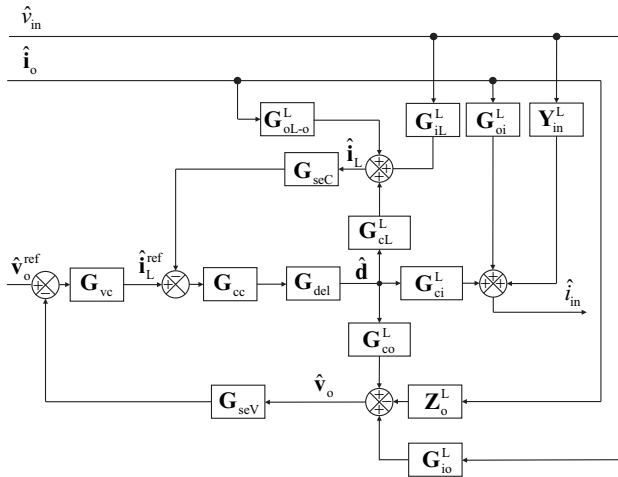


Figure 11. Control block diagram of the closed-loop system.

change in the voltage reference d-component as the R-load is used. The step is from 155 V to the nominal amplitude 169,7 V. There is no overshoot or oscillation in the response. The response with the RLC-load as the controller remains unchanged is also shown in Fig. 12. A significant overshoot and decaying oscillation is present in the response.

The model is used to retune the controllers so that a proper step-response is achieved with the RLC-load. The current controller pole location is changed to 100 Hz and the new gain is 24.8 dB. The voltage controller zero is moved to 5 Hz, two poles are located at 60 Hz and the new gain is 24.1 dB. Fig. 13 shows the predicted and HIL-simulated voltage loop gains. The phase margin is  $58.2^\circ$  at 20.6 Hz. The gain margin is 14 dB at 129 Hz. The step response in Fig. 14 is good, as the higher phase margin than with previous controller tuning implies.

The previous analysis shows that the proposed model can be used to analyze the effect of different loads on the control dynamics. Frequency responses of the load-affected transfer functions can be used to predict the time-domain behavior and to design the controllers according

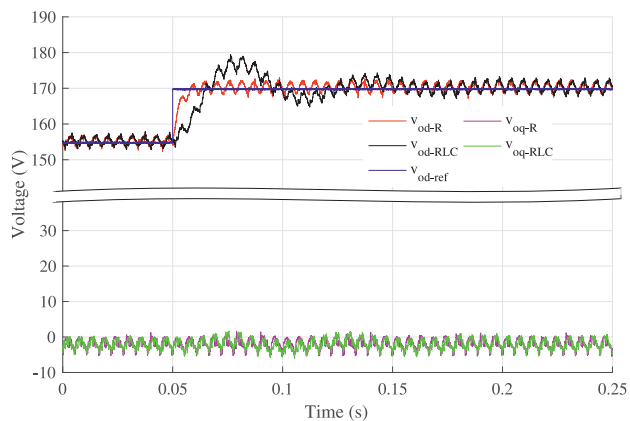


Figure 12. Typhoon HIL simulation of output voltage d and q-components step response to a reference step for the R-load and for the RLC-load.

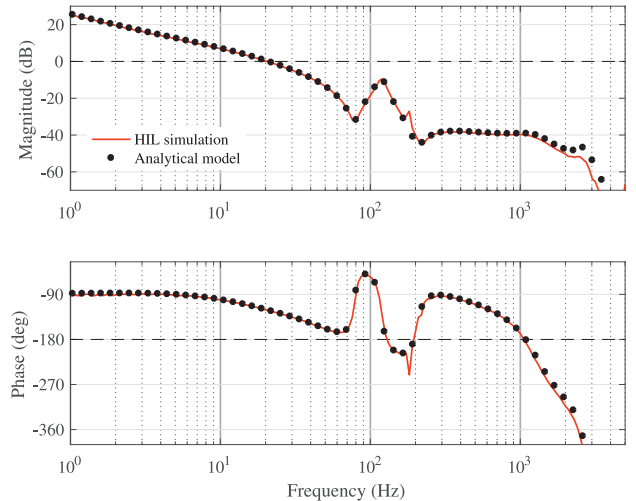


Figure 13. Bode plot of simulated and predicted voltage loop gain with the controller that is tuned for the RLC-load.

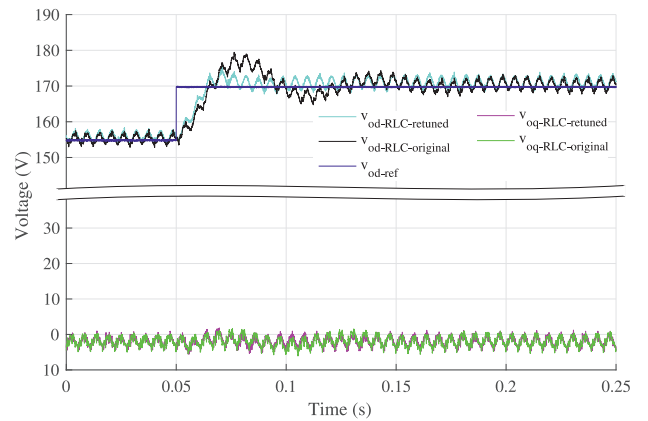


Figure 14. Typhoon HIL simulation of output voltage d and q-component step responses to a reference step with the RLC-load with the original controller and the controller retuned for RLC-load.

to a specific load or a worst-case scenario.

## V. CONCLUSION

This paper proposes a method to model unterminated dynamics of a grid-forming inverter. The effect of a non-ideal load is included in the model by calculating, how the load impedance affects the output dynamics. Furthermore, the unterminated model of the grid-forming inverter includes the output impedance that is required to calculate the load-affected model and an important tool in the stability analysis of interconnected systems.

The HIL measurements provided in this paper confirm that the frequency response analysis is a powerful tool for predicting the time-domain response of the grid-forming inverter under distinct loads. One possible application of the proposed modeling technique is to tune the controller according to a specific load so that a desired time-domain response is achieved. The model can be also used to examine worst-case load conditions. The load effect can be also removed from the measured load affected frequency response and the unterminated model can be

verified. Future work will concentrate on the on the load-affected dynamics in the case of an active load, such as an active rectifier.

#### APPENDIX A

Eq. (36) shows the grid-side inductor admittance state-space coefficient matrices.

$$\mathbf{A}_{L2} = \begin{bmatrix} \frac{-r_{L2}}{L_2} & \omega_s \\ -\omega_s & \frac{-r_{L2}}{L_2} \end{bmatrix} \quad \mathbf{B}_{L2} = \begin{bmatrix} \frac{1}{L_2} & 0 \\ 0 & \frac{1}{L_2} \end{bmatrix}$$

$$\mathbf{C}_{L2} = \begin{bmatrix} 1 & 0 \\ 0 & 1 \end{bmatrix} \quad \mathbf{D}_{L2} = \begin{bmatrix} 0 & 0 \\ 0 & 0 \end{bmatrix} \quad (36)$$

#### APPENDIX B

Eq. (37) shows the RLC-load admittance state-space coefficient matrices.

$$\mathbf{A}_{RLC} = \begin{bmatrix} \frac{-r_{LL}}{L_L} & \omega_s & 0 & 0 \\ -\omega_s & \frac{-r_{LL}}{L_L} & 0 & 0 \\ 0 & 0 & \frac{-1}{C_L r_{CL}} & \omega_s \\ 0 & 0 & -\omega_s & \frac{-1}{C_L r_{CL}} \end{bmatrix}$$

$$\mathbf{B}_{RLC} = \begin{bmatrix} \frac{1}{L_L} & 0 \\ 0 & \frac{1}{L_L} \\ \frac{1}{C_L} & 0 \\ 0 & \frac{1}{C_L} \end{bmatrix} \quad \mathbf{C}_{RLC} = \begin{bmatrix} 1 & 0 & \frac{-1}{r_{CL}} & 0 \\ 0 & 1 & 0 & \frac{-1}{r_{CL}} \end{bmatrix}$$

$$\mathbf{D}_{RLC} = \begin{bmatrix} \frac{1}{R_L} + \frac{1}{r_{CL}} & 0 \\ 0 & \frac{1}{R_L} + \frac{1}{r_{CL}} \end{bmatrix} \quad (37)$$

#### REFERENCES

- [1] I. J. o. Balaguer, "Control for grid-connected and intentional islanding operations of distributed power generation," *IEEE Trans. Ind. Electron.*, vol. 58, no. 1, pp. 147–157, 2011.
- [2] M. Rasheduzzaman, J. A. Mueller, and J. W. Kimball, "An accurate small-signal model of inverter-dominated islanded microgrids using dq reference frame," *IEEE Trans. Emerg. Sel. Topics Power Electron.*, vol. 2, no. 4, pp. 1070–1080, 2014.
- [3] J. Rocabert *et al.*, "Control of power converters in AC microgrids," *IEEE Trans. Power Electron.*, vol. 27, no. 11, pp. 4734–4749, nov 2012.
- [4] T. Suntio, T. Messo, and J. Puukko, *Power Electronic Converters: Dynamics and Control in Conventional and Renewable Energy Applications*. Wiley VCH, 2017.
- [5] B. Wen *et al.*, "Modeling the output impedance of three-phase uninterruptible power supply in D-Q frame," in *2014 IEEE Energy Conversion Congress and Exposition (ECCE)*. IEEE, 2014, pp. 163–169.
- [6] S. Lissandron *et al.*, "Experimental validation for impedance-based small-signal stability analysis of single-phase interconnected power systems with grid-feeding inverters," *IEEE Journal of Emerging and Selected Topics in Power Electronics*, vol. 4, no. 1, pp. 103–115, 2016.
- [7] T. Roinila, T. Messo, and E. Santi, "Mimo-identification techniques for rapid impedance-based stability assessment of three phase systems in DQ domain," *IEEE Trans. Power Electron.*, vol. 33, no. 5, pp. 1–1, 2017.
- [8] B. Wen *et al.*, "AC stability analysis and dq frame impedance specifications in power-electronics-based distributed power systems," *IEEE Trans. Emerg. Sel. Topics Power Electron.*, vol. 5, no. 4, pp. 1455–1465, dec 2017.
- [9] B. Wen and othe, "Impedance-based analysis of grid-synchronization stability for three-phase paralleled converters," *IEEE Trans. Power Electron.*, vol. 31, no. 1, pp. 26–38, 2016.
- [10] M. Ramezani, S. Li, and S. Golestan, "Analysis and controller design for stand-alone vsis in synchronous reference frame," *IET Power Electron.*, vol. 10, no. 9, pp. 1003–1012, 2017.
- [11] J. M. Guerrero *et al.*, "Output impedance design of parallel-connected UPS inverters with wireless load-sharing control," *IEEE Trans. Ind. Electron.*, vol. 52, no. 4, pp. 1126–1135, 2005.
- [12] A. Yazdani, "Control of an islanded distributed energy resource unit with load compensating feed-forward," in *2008 IEEE Power and Energy Society General Meeting - Conversion and Delivery of Electrical Energy in the 21st Century*. IEEE, 2008, pp. 1–7.
- [13] R. J. Vijayan, S. Ch, and R. Roy, "Dynamic modeling of microgrid for grid connected and intentional islanding operation," in *2012 International Conference on Advances in Power Conversion and Energy Technologies (APCET)*. IEEE, aug 2012, pp. 1–6.
- [14] T. Vandoorn *et al.*, "Theoretical analysis and experimental validation of single-phase direct versus cascade voltage control in islanded microgrids," *IEEE Trans. Ind. Electron.*, vol. 60, no. 2, pp. 789–798, 2013.
- [15] R. D. Middlebrook, "Small-signal modeling of pulse-width modulated switched-mode power converters," *Proc. IEEE*, vol. 76, no. 4, pp. 343–354, 1988.
- [16] A. Aapro *et al.*, "Effect of active damping on output impedance of three-phase grid-connected converter," *IEEE Trans. Ind. Electron.*, vol. PP, no. 99, pp. 1–1, 2017.
- [17] J. Puukko and T. Suntio, "Modelling the effect of non-ideal load in three-phase converter dynamics," *Electronics Letters*, vol. 48, no. 7, p. 402, 2012.
- [18] T. Suntio, *Dynamic Profile of Switched-Mode Converter: Modeling, Analysis and Control*. Weinheim, Germany: Wiley, 2009.
- [19] B. Wen and other, "D-Q impedance specification for balanced three-phase AC distributed power system," in *2015 IEEE Applied Power Electronics Conference and Exposition (APEC)*. IEEE, 2015, pp. 2757–2771.
- [20] R. Burgos *et al.*, "On the ac stability of high power factor three-phase rectifiers," in *2010 IEEE Energy Conversion Congress and Exposition*. IEEE, 2010, pp. 2047–2054.
- [21] A. Rygg *et al.*, "On the equivalence and impact on stability of impedance modelling of power electronic converters in different domains," *IEEE Trans. Emerg. Sel. Topics Power Electron.*, no. 4, pp. 1–1, 2017.
- [22] J. Chen and J. Chen, "Stability analysis and parameters optimization of islanded microgrid with both ideal and dynamic constant power loads," *IEEE Trans. Ind. Electron.*, vol. 65, no. 4, pp. 1–1, 2017.
- [23] Poh Chiang Loh *et al.*, "A comparative analysis of multiloop voltage regulation strategies for single and three-phase UPS systems," *IEEE Trans. Power Electron.*, vol. 18, no. 5, pp. 1176–1185, 2003.
- [24] P. Loh and D. Holmes, "Analysis of multiloop control strategies for LC/CL/LCL-filtered voltage-source and current-source inverters," *IEEE Trans. Ind. Appl.*, vol. 41, no. 2, pp. 644–654, 2005.